

Structure and elasticity of cubic Fe-Si alloys at high pressures

E. Edmund ^{*}, D. Antonangeli, F. Decremps, G. Morard, S. Ayrinhac, M. Gauthier , and E. Boulard
*Institut de Minéralogie, de Physique des Matériaux et de Cosmochimie, Sorbonne Université, UMR CNRS 7590,
 IRD, Muséum National d'Histoire Naturelle, Paris 75005, France*

M. Mezouar and M. Hanfland
ESRF, Grenoble 38000, France

N. Guignot
Synchrotron SOLEIL, Saint-Aubin 91192, France

 (Received 5 August 2019; revised manuscript received 23 September 2019; published 22 October 2019)

Using a combination of picosecond acoustics and synchrotron x-ray diffraction, the sound velocities and equations of state of Fe-Si alloys have been determined over a wide range of compositions (10–29 at. % Si) and pressures (up to 65 GPa) under quasihydrostatic conditions. We observe marked variation in the elastic properties of the alloys depending on synthesis method and degree of Si ordering. In particular, it is observed that there is a sharp change in the density dependence of the sound velocities which coincides with the observation of long-range ordering by diffraction methods. This change in elasticity is probably due to a change in bond character of the Fe-Si alloy. Furthermore, the bcc-hcp transition in these alloys has been mapped to high pressures and Si contents. We observed that the onset of the transition changes by more than 6 GPa per at. % for alloys containing more than ~ 15 at. % Si.

DOI: [10.1103/PhysRevB.100.134105](https://doi.org/10.1103/PhysRevB.100.134105)

I. INTRODUCTION

The Fe-Si system underpins an important class of technological materials, providing a low-cost route to materials with high corrosion resistance and mechanical durability, combined with widely tunable magnetic and electronic properties [1]. Indeed, up to 10–12 at. % Si is added to Fe to form silicon steels, widely used for electrical and energy conversion applications (e.g., [2,3]). More Si-rich compounds have shown promise for applications ranging from photovoltaics to microelectronics (e.g., [4]). While classical pulse-echo ultrasonics and x-ray diffraction investigations have established a clear picture of the variation of elasticity and structure with Si content in alloys containing up to at least 50 at. % Si (e.g., [5–8]), there is still no consensus on the physical origins of the observed variations in this system [4,9–11]. *Ab initio* calculations indicate that changes in magnetic structure are a key driver of structural stability in the Fe-rich Fe-Si phase diagram [9,10]. However, there is debate over whether the anomalous elastic behavior at low Si content and the observed ductile-brittle transition in this system are driven by magnetic or electronic effects [11].

Fe alloys with up to 25 at. % Si display a series of solid solutions based on the bcc Fe structural motif at ambient temperature and pressure [6]. While such materials are ductile for concentrations up to about 8 at. % Si, they are exceedingly brittle and, consequently, unworkable at higher concentrations, in spite of their improved magnetic properties

as electrical steels (e.g., [12]). In order to retain the mechanical properties of dilute Fe-Si alloys while providing magnetic properties accessible at only higher Si concentrations, modern studies of the Fe-Si system have increasingly moved towards using out-of-equilibrium synthesis methods (e.g., [13,14]), such as melt spinning, mechanical annealing, and physical vapor deposition (PVD) [15]. Through these methods, it has been possible to strongly modify the Fe-Si phase diagram, synthesizing structures well beyond their thermodynamic stability fields. However, there are virtually no experimental investigations into the elastic properties of Fe-Si alloys synthesized by such means or their behavior under pressure. Such information plays a key role in understanding the interdependence of structure, bonding, and magnetism in this system. Indeed, the variation of the lattice parameter (and consequently volume) with Si concentration is linked to changes in magnetic structure in this system (e.g., [16]), and compressional sound velocities (denoted here as V_P) are highly sensitive to changes in elastic moduli, the second derivative of free energy with strain. Thus, combined investigations of V and V_P under pressure provide an accurate probe for assessing compositional and structural variations in alloy interatomic potentials.

In order to better understand the role of chemical ordering on the physical properties of Fe-rich Fe-Si alloys (with less than 50 at. % Si), a series of Fe-Si alloys synthesized by melt spinning and PVD (Si content up to 29 at. %) are here characterized using synchrotron x-ray diffraction and picosecond acoustics (PA) up to 65 GPa under quasihydrostatic conditions. Such measurements allow for the determination of unit cell volume and V_P at both ambient and high pressures,

^{*}eric.edmund@upmc.fr

placing tight constraints on not only ambient-pressure elastic parameters but also their volume and structure dependence.

II. METHODS

Experiments were performed using Fe-Si alloys measured by a scanning electron microscope (SEM) to contain 9.8(5), 14.7(2.0), 16.4(2.0), 18.6(2.0), 21.3(2.0), and 28.9(2.0) at. % Si. These alloys are referred to hereafter as Fe- x Si where $x = 10, 15, 16, 19, 21, 29$, the rounded concentration of each alloy in atomic percent. Fe-10Si was synthesized by melt spinning at Institut de Chimie et des Matériaux de Paris-Est (Paris, France) following the experimental protocol outlined in Morard *et al.* [17]. All other alloys were synthesized by PVD either by Dephis or at the Institut de Mineralogie, de Physique des Matériaux et de Cosmochimie (IMPMC; Paris, France). All alloys were measured by synchrotron x-ray diffraction (XRD) both at ambient conditions and at high pressures, except in the case of Fe-16Si, for which only ambient-pressure characterization was performed, and are observed to be single phase, fully crystallized materials. PVD samples were further characterized at ambient pressure by profilometry and picosecond acoustics, allowing for the determination of reference values of V_P of these alloys at ambient conditions to an error of $\leq 1\%$ for Fe-(16,19,21)Si and $\leq 2\%$ for Fe-(15,29)Si. The ambient pressure V_P and error in V_P for Fe-10Si were determined using literature elastic constants [7] as discussed in Edmund *et al.* [18].

Measurements at high pressures were performed using Le Toullec-type membrane-driven diamond anvil cells (DACs), equipped with diamonds with culet diameters ranging from 350 to 100 μm and 200- μm -thick rhenium gaskets. The rhenium gaskets were indented to thicknesses of 60 to 20 μm depending on the diamond culet diameter. A femtosecond pulsed laser was used to machine a hole in the center of the indented gasket, roughly half the diameter of the diamond culet, to act as the sample chamber. Ne was used as the pressure-transmitting medium (PTM), ensuring quasihydrostatic compression. The sample chamber was stable to the highest achieved pressures of the present study, without contact between the sample, gasket, and pressure calibrant during any experimental run.

A. X-ray diffraction

For all diffraction experiments, the sample chamber contained Mo or Pt as the pressure calibrant. For the Mo equation of state we used the elastic parameters reported in Litasov *et al.* [19] [$K_0 = 260$ GPa, $K' = 4.19(5)$] and the reference V_0 of Mo ($V_0 = 31.17 \text{ \AA}^3$ [20]). For the Pt equation of state we used that proposed by Dewaele *et al.* [21], $V_0 = 60.38 \text{ \AA}^3$, $K_0 = 277.3$ GPa, $K' = 5.12$. Both pressure scales are in good agreement where there is overlap in data sets and are observed to be consistent with the ruby fluorescence scale used for PA measurements [22].

All alloys investigated by XRD were loaded as foils, mechanically etched either from a glass substrate in the case of PVD samples or from a larger alloy ribbon in the case of Fe-10Si. On the basis of SEM analysis of the starting materials, the grain size of the alloys was less than 200 nm.

Williamson-Hall analysis of ambient-pressure diffraction measurements has shown that crystallite size varies from alloy to alloy; however, this is not observed to correlate with the reported compositional variations in elasticity presented in this study.

Synchrotron XRD measurements were carried out on beamline Pression Structure Imagerie par Contraste à Haute Énergie (PSICHÉ) at Synchrotron Soleil and on beamlines ID15b and ID27 at the European Synchrotron Radiation Facility (ESRF). All XRD measurements were performed in transmission geometry. At PSICHÉ, the x-ray wavelength was $\lambda = 0.3738$ nm, and the beam was focused to approximately $15 \times 10 \mu\text{m}^2$ (horizontal by vertical, $H \times V$) full width at half maximum (FWHM). At this beamline, collection times were between 30 and 60 s, and the cell was rotated $\pm 5^\circ$ during collection to improve orientational averaging. At ID15b, the x-ray wavelength was $\lambda = 0.411545$ nm, the beam was focused to about $6 \times 6 \mu\text{m}^2$ $H \times V$ FWHM, and collection times were about 5 s, without rotation of the cell. At ID27, the x-ray wavelength was $\lambda = 0.3738$ nm, focused to $\sim 3 \times 3 \mu\text{m}^2$ ($H \times V$ FWHM), and collection times were 30–60 s.

Diffraction images were calibrated against a CeO₂ standard for measurements performed at PSICHE and ID27 or were calibrated against an Si standard for those performed at ID15b. The images were then azimuthally integrated using DIOPAS [23] to make diffraction patterns, which were then fit using JANA2006 [24] or PDINDEXER [25].

B. Picosecond acoustics

Pump-probe time-resolved reflectivity measurements were performed at IMPMC [26] in order to determine the acoustic travel time of the Fe-Si alloys investigated. A Ti:sapphire laser beam ($\lambda = 800$ nm, pulse duration ~ 100 fs) is split into two optical paths (with intensity split roughly 80:20 pump:probe): a pump beam and a probe beam. The pump and probe beams are focused on opposite, parallel surfaces of the flat metallic sample loaded in the DAC. The pump beam has a repetition rate of 80 MHz modulated at 1 MHz through the use of an acousto-optic modulator for lock-in noise rejection. The absorption of the pump beam at the sample surface generates a small thermal stress, which relaxes by launching elastic waves that propagate throughout the sample. The probe beam is employed to measure the time-resolved reflectivity of the opposite sample surface. The reflected signal from the probe beam is passed through an interferometer and used to determine the phase shift of the reflectivity, which is observed to change abruptly upon the arrival of the elastic wave at the surface. To resume, the pump beam generates bulk waves, and the probe beam measures sample reflectivity as a function of time in order to detect the arrival of compressional bulk waves at the opposite face of the sample.

For the preparation of DAC experiments, samples synthesized by PVD were mechanically etched from the glass substrate that they were deposited on. Sample diameters were between 20 and 50 μm , depending on target pressures and sample chamber size. Measured travel times at different locations on a given sample were observed to be uniform at both ambient and high pressures. For Fe-10Si, some scatter was

observed in travel times due to texturing of the initial sample during loading, described in Edmund *et al.* [18].

The ruby fluorescence method was employed [27] for the determination of pressure during experimental runs, using the pressure calibration of Sokolova *et al.* [22]. Ruby fluorescence was measured before and after each measurement. Pressure drift was about 0.1 GPa below 10 GPa, up to 0.5 GPa between 10 and 30 GPa, and up to 2 GPa at the highest pressures in this study. As the difference in pressure before and after measurement is the largest source of experimental uncertainty in pressure, this was used as the error bar in pressure for the determination of sound velocities.

V_p of the alloys are simply determined by dividing a sample's thickness e by the measured acoustic travel time. Here e was determined through the measurement of the initial travel time of the sample loaded in the DAC before gas loading, combined with the known sound velocity of the starting material at ambient pressure, and was assumed to scale as $e_0(V_0/V)^{1/3}$ under pressure (the assumption of hydrostatic compression of the sample).

III. RESULTS

A. X-ray diffraction

Pressure-volume (P - V) equations of state (EOSs) of each alloy were determined at high pressures over the entire bcc/B2 pressure stability field, except in the case of Fe-29Si, where an hcp transition was not observed. The measured P - V relations were fit with both Rydberg-Vinet (RV) and third-order Birch-Murnaghan (3BM) EOSs [28,29]:

$$P(V) = \frac{3}{2}K_0 \left(\frac{1-\eta^2}{\eta^7} \right) \left\{ 1 + \frac{3}{4}(K' - 4) \left(\frac{1-\eta^2}{\eta^2} \right) \right\}, \quad (1)$$

$$P(V) = 3K_0 \left(\frac{1-\eta}{\eta^2} \right) \exp \left[\frac{3}{2}(K' - 1)(1-\eta) \right]. \quad (2)$$

In Eqs. (1) and (2), K_0 and K' refer to the bulk modulus (in GPa) and its pressure derivative (dimensionless), respectively, while $\eta = \frac{V}{V_0}^{1/3}$, where V and V_0 are the high-pressure and ambient-pressure unit cell volumes (with units of $\text{\AA}^3/\text{atom}$).

For the determination of sound velocities, the 3BM formalism and elastic parameters were used in data analysis; however, we stress that the difference in fitted elastic parameters for the two choices of EOSs is minor. Figure 1 shows the present data set alongside selected literature studies.

Out of the DAC studies performed on this system we excluded from Fig. 1 results obtained using pressure-transmitting media which are nonhydrostatic at high pressures. Furthermore, for consistency, results of studies performed in Ne or employing laser annealing to reduce nonhydrostatic stress are shown [31–34] and are refitted using pressure values which have been rescaled to modern calibrations consistent with the present data set and studies employing “absolute-pressure” methods [35]. The significant discrepancies among the various studies can be reconciled by noting systematic differences due to the employed pressure calibrations.

Table I summarizes the fitted EOS elastic parameters from the present study while Supplemental Table S2 summarizes

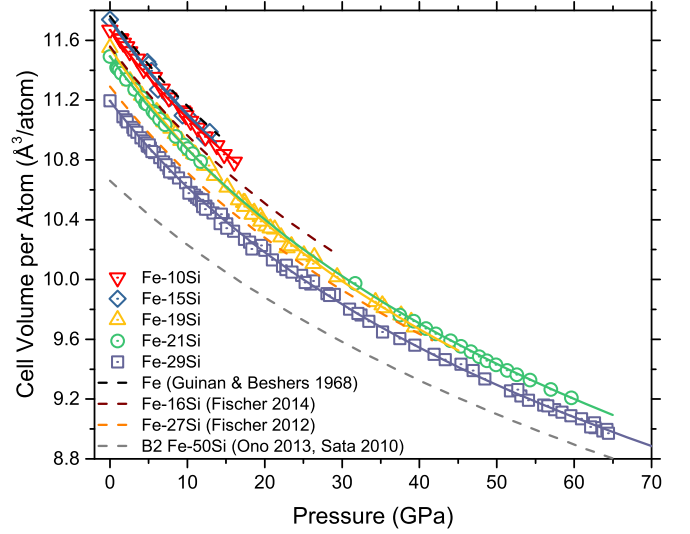


FIG. 1. Cell volume per atom vs pressure for the Fe-Si alloys investigated here and selected literature [30–34]. All data points presented here have error bars smaller than the symbols, with the exception of some points from Fe-15Si. All literature results except those of Guinan and Beshers [30] were rescaled using pressure scales consistent with the present study.

the EOS parameters reported in DAC and high-pressure pulse-echo ultrasonics literature. It is seen that there is general agreement between refit static data, the present study, and ultrasonics for a number of compositions. However, in the present study there are clear discrepancies in the EOS parameters (and compressional behavior) of Fe-(15,19,21)Si alloys relative to the trends in the literature. For alloys, V_0 and its error have been fixed to the value determined at ambient pressure, with the exception of Fe-10Si, for which some fits were performed with all parameters free. In the case of Fe-15Si, K' was fixed to 5 based on the observation that Fe-(19,21,29)Si

TABLE I. Table of EOS parameters from the present study. Supplemental Table S1 (see the Supplemental Material [36]) indicates the pressure standard employed and the beamline used for measurements. Bold numbers were fixed during the fitting process. Literature EOS parameters are presented in Table S2.

| Alloy | Formalism | V_0 ($\text{\AA}^3/\text{atom}$) | K_0 (GPa) | K' |
|---------|-----------|--------------------------------------|-------------|----------|
| Fe-10Si | 3BM | 11.70(1) | 166.3(6.7) | 4(1) |
| | 3BM | 11.67(2) | 168.9(1.2) | 5 |
| | RV | 11.70(1) | 166.3(6.9) | 4(1) |
| | RV | 11.67(2) | 169.2(1.2) | 5 |
| Fe-15Si | 3BM | 11.74(2) | 156.0(3.1) | 5 |
| | RV | 11.74(2) | 156.0(3.1) | 5 |
| Fe-19Si | 3BM | 11.55(2) | 142.6(1.5) | 5.1(2) |
| | RV | 11.55(2) | 141.9(1.5) | 5.3(2) |
| Fe-21Si | 3BM | 11.49(2) | 157.5(1.0) | 5.0(1) |
| | RV | 11.49(2) | 156.3(1.0) | 4.8(1) |
| Fe-29Si | 3BM | 11.20(2) | 164.1(1.2) | 5.3(1) |
| | RV | 11.20(2) | 162.8(1.2) | 5.5(1) |

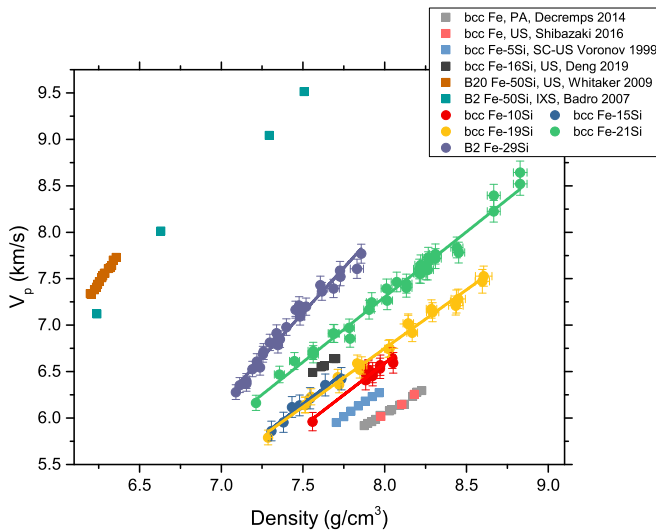


FIG. 2. Compressional velocity V_p vs density ρ from the present study and selected literature [35,38,41–44]. In the legend, IXS = inelastic x-ray scattering, US = polycrystal ultrasonics, SC-US = single-crystal ultrasonics. Derived shear velocity V_s - ρ relations can be seen in Supplemental Fig. S2. US and PA studies on bcc-Fe [38,42] are observed to be in good agreement at high pressures, as are velocity measurements on hcp Fe performed by techniques covering the megahertz to terahertz frequency range [45]. Thus, it is expected that differences in sound velocities from these techniques due to frequency dispersion are small within experimental uncertainties.

exhibit comparable values of K' ; however, the fitted value of K_0 for this data set is not sensitive to variation of K' .

B. Picosecond acoustics

The sound velocities of Fe-Si alloys were determined up to the bcc-hcp transition for all alloys except Fe-29Si, where a transition was not observed. In the case of pure Fe, pretransition elastic softening has not been reported (e.g., [37,38]). However, for alloys of Fe-(19,21)Si we observe nonlinear variations in V_p a few gigapascals before the onset of the structural transition determined by XRD, attributed to shear softening of the alloy before the bcc-hcp transition. While all alloys studied appear to systematically exhibit different behavior from Fe during the bcc-hcp transition region, the pressure stability field of Fe-10Si and Fe-15Si was too small to unambiguously confirm the existence of pretransition softening. Regardless, bcc-phase data points close to the bcc-hcp transition were omitted from analysis of velocity-density

relations. While velocity determination is dependent on the assumption that sample thickness varies only with unit cell volume, elastic or plastic deformation of the sample is likely negligible at these conditions. The highest-pressure velocity points used in the velocity-density relations of this study (Fig. 2) result in derived Young's moduli of ~ 340 GPa for Fe-19Si at $P = 36.3$ and ~ 490 GPa for Fe-21Si at $P = 51.9$ GPa. At the same pressures, the shear strength of Ne is less than 1–2 GPa [39], and thus, deformation of the sample by the Ne PTM is not likely.

In the quasiharmonic approximation, phonon energies are proportional to $1/V$, which results in a linear relationship between V_p and density, also referred to as Birch's law [40]. The variation of sound velocities with density encodes the material-specific elastic response to compression. Consequently, variation in the slope of the velocity-density plot provides a sensitive probe to changes in the Fe alloy interatomic potential. Figure 2 shows the velocity-density relations from the present work and selected literature. It is observed that from Fe to Fe-21Si there is little difference in the general trends of the velocity-density plots; these bcc alloys are roughly parallel to each other, with the primary differences arising from changes in the initial density ρ_0 and V_p ($V_{p,0}$). Alloys in either the B2 ($Pm\bar{3}m$) or B20 ($P2_13$) structure show a significant variation of the slope of V_p vs density, indicating modifications in the interatomic potential, discussed further in Sec. IV D. Linear fits to both the V_p - ρ relations and derived shear velocity V_s - ρ relations are shown in Table II.

IV. DISCUSSION

A. Cell volume vs Si content at ambient pressure

The low-temperature (< 1000 K), ambient-pressure binary Fe-FeSi phase diagram comprises four main phases: bcc Fe- x Si (space group: $Im\bar{3}m$), B2 Fe- x Si (space group: $Pm\bar{3}m$), DO3 Fe- x Si (space group: $Fm\bar{3}m$), and B20 FeSi (space group: $P2_13$) [6]. While end member B20 FeSi is approximately stoichiometric, for a wide range of more Fe-rich compositions (about 0–30 at. % Si), the phase diagram exhibits bcc, B2, and DO3-type solid solutions, depending on the synthesis conditions, Si concentration, and the mechanical or thermal treatment of the material [46]. As a result, these alloys display varied magnetic properties, and such properties strongly depend on the process by which the samples were made. Both melt spinning and PVD are techniques which tend to suppress the formation of ordered phases within Fe-Si alloys, but through different mechanisms. With melt spinning techniques, a homogeneous, molten liquid is ejected through a

TABLE II. Table of velocity-density (V_p and derived V_s) relations from the present study. Ambient-pressure densities ρ_{amb} are derived from the measured molar mass and ambient-pressure unit cell volume.

| Alloy | ρ_{amb} (g cm $^{-3}$) | $dV_p/d\rho$ (km s $^{-1}$ cm 3 g $^{-1}$) | V_{p0} (km s $^{-1}$) | $dV_s/d\rho$ (km s $^{-1}$ cm 3 g $^{-1}$) | V_{s0} (km s $^{-1}$) |
|---------|-------------------------------------|---|-----------------------------|---|--------------------------|
| Fe-10Si | 7.56(1) | 1.36(10) | −4.27(76) | 0.57(14) | −1.2(1.1) |
| Fe-15Si | 7.31(1) | 1.35(11) | −4.01(84) | 0.58(17) | −1.1(1.3) |
| Fe-19Si | 7.30(1) | 1.26(3) | −3.33(24) | 0.46(4) | −0.1(3) |
| Fe-21Si | 7.21(1) | 1.40(3) | −3.91(26) | 0.68(4) | −1.4(3) |
| Fe-29Si | 7.09(1) | 1.94(6) | −7.40(50) | 1.16(9) | −4.7(6) |

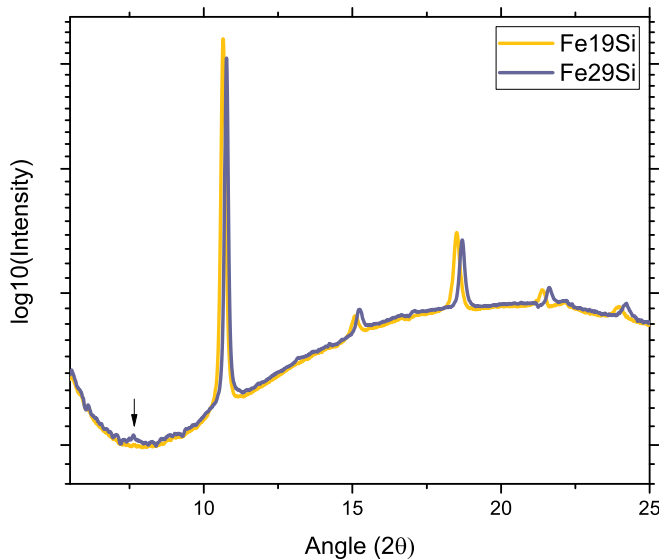


FIG. 3. Diffraction patterns of Fe-19Si and Fe-29Si both measured under the same experimental conditions at beamline PSICHE. The black arrow shows a weak reflection at low angle for Fe-29Si, the signature of structural ordering of the Si atoms in the alloy. An extended figure including all Fe-Si alloys is shown in Supplemental Fig. S3.

pressurized quartz nozzle on a spinning Cu alloy wheel (e.g., [17]), suppressing the migration of solutes within an alloy during cooling. In the case of PVD, the temperature of sample synthesis is sufficiently low that kinetics prevent the formation of long-range Si ordering [3]. Thus, both techniques can hamper the formation of the ordered B2 and DO₃ structures, as shown in Fig. 3. In the present study, the phase content of all alloys has been determined via XRD at ambient pressure.

At very low Si contents (approximately less than 8 at. %) the Fe-*x*Si alloys are primarily composed of a bcc solid solution, with Si atoms randomly replacing Fe with no site preference. Using classical methods for sample synthesis, B2-type ordering occurs for samples above 7–8 at. % Si, and DO₃ occurs above 10 at. % Si [47]. However, in the present study, through the use of PVD methods the formation of Si ordering was suppressed in all alloys containing up to 21 at. % Si, above which a B2 structure is observed.

Figure 4 shows that the unit cell volume of Fe-Si alloys decreases linearly with Si concentration, with two regimes from 0 to 8 at. % Si and from about 11 to 30 at. % Si with an intermediary region between the two (8–11 at. % Si) where the literature is somewhat scattered. Linear fits to the volume (in Å³ per atom) vs atomic percent data of the available literature (omitting samples synthesized by out-of-equilibrium methods) give relations of $V = 11.780(2) - 0.0088(3)x$ from 0 to 8 at. % Si and $V = 11.936(6) - 0.0255(3)x$ from 11 to 30 at. % Si. It is observed that while Fe-10Si and Fe-29Si measured here are both consistent with literature trends, all alloys intermediate to these compositions exhibit systematically higher volumes at the same concentration relative to the equilibrium literature. The observed deviations from equilibrium *V* vs atomic percent relations are likely driven by the differences in structural ordering as for bcc alloys

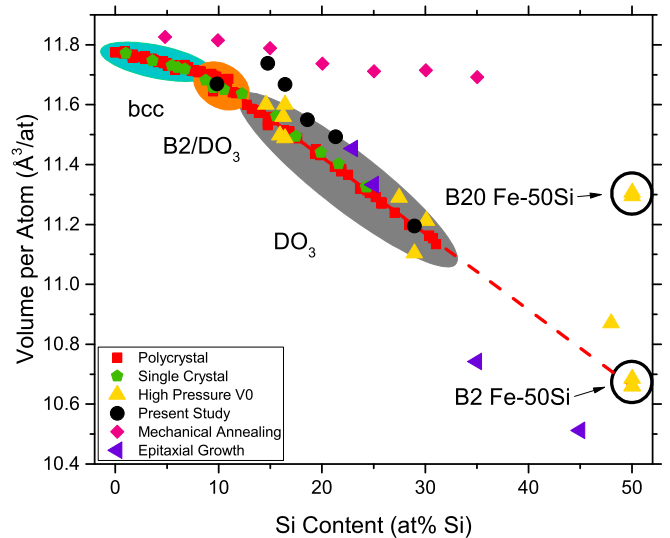


FIG. 4. Volume per atom at ambient pressure vs alloy Si concentration of the present work and available literature. Polycrystal denotes XRD investigations of polycrystalline samples (omitting those performed for high-pressure studies) [5,6,14,48–50]. Results of Jette and Greiner [48], Phragmén [5], Farquhar *et al.* [6] were converted from Cu X units [51]. Single crystal denotes single-crystal XRD studies [52,53]. High pressure V0 denotes ambient-pressure measurements from high-*P* studies [31,32,35,54–56]. Volumes from other out-of-equilibrium techniques (mechanical annealing [57] and epitaxial growth [58]) are shown for comparison.

the volume decreases more slowly with Si content than for DO₃-type alloys.

While Fe and Si have similar atomic sizes within an Fe-Si lattice, the volume per atom of bcc Fe is significantly larger than that of diamond Si due to magnetic interactions of Fe *d* electrons. Fe atoms in bcc Fe have unpaired *d* electrons which generate a local magnetic moment, which in turn causes a repulsive interaction between these atoms. *Ab initio* calculations of bcc Fe either including or excluding magnetic effects have shown that a fictive nonmagnetic bcc Fe lattice exhibits a significantly reduced unit cell volume relative to experimental determinations (e.g., [59]). By contrast Si has no *d* electrons and is nonmagnetic, and as a consequence, alloying Fe with Si screens magnetic interactions between Fe atoms, which can weaken the bulk magnetic moment of the resulting alloy [9,10].

The general trend of decreasing the lattice constant with Si shown in Fig. 4 is due to the weakening of the average magnetic moment of the alloy. While the bulk magnetic moment decreases weakly from 0 to ~8 at. % Si [60], the kink in the volume-Si content curve at 8–11 at. % Si arises from a splitting of the different crystallographic locations of Fe within the Fe-Si alloy into magnetic states with differing moments, coinciding with the onset of DO₃-type ordering [9]. This in turn alters how the magnetism varies with Si content. It is interesting to note that while the volume per atom of B2 Fe-50Si is markedly different from the trends established above, the volume of the high-pressure B2 phase of this composition agrees well with extrapolations from the stability field of DO₃-structured alloys.

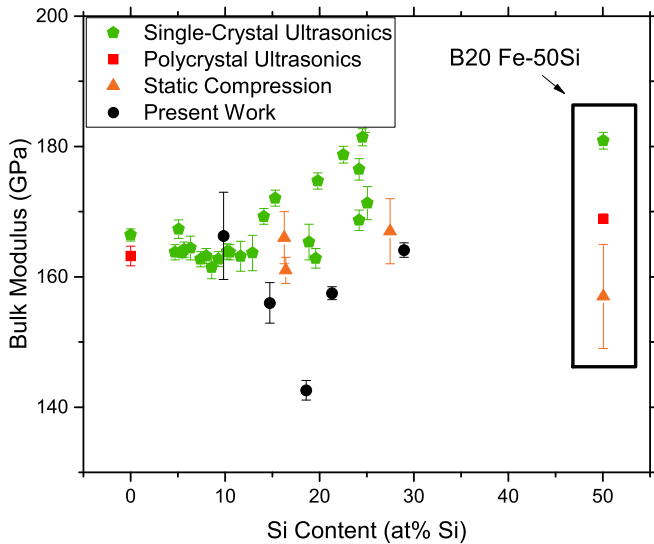


FIG. 5. Bulk modulus at ambient pressure K_0 vs Si content determined in the present study and selected experimental literature [7,8,30–32,35,41,61–63]. The difference between isothermal and adiabatic bulk moduli has not been taken into account, as at 300 K this difference is about 2–3 GPa when using thermoelastic parameters from the literature [31,64,65].

B. Bulk modulus vs Si content

It has been shown experimentally that the elastic moduli of Fe-Si solid solutions undergo significant changes in behavior in the vicinity of the DO_3 transition. The bulk moduli K_0 in particular have been reported to decrease with increasing Si content up to the DO_3 transition pressure, followed by an increase in K_0 with increasing Si concentration in the stability field of the DO_3 structure (e.g., [7,8]).

The results of *ab initio* calculations generally agree that the initial reduction of K_0 has an electronic origin [9], related to the screening of d - d interactions of Fe sites [10,11]. However, there is still debate over whether the recovery of K_0 in the DO_3 stability field is due to a magnetovolume effect (the relative change in the magnetic moment and volume with Si content) [10] or increased bond covalency due to the formation of long-range Si ordering [11].

Figure 5 shows the K_0 values determined in the present study alongside the DAC literature [31–34] (isothermal K_0) and the results of single-crystal and polycrystalline ultrasonics measurements [7,8,30,35,41,42,62,63] (adiabatic K_0). It is observed that while there is significant scatter across ultrasonic determinations of K_0 in the DO_3 region, DAC measurements tend to support a weaker trend in K_0 vs Si content in the DO_3 region.

In the present study, it has been observed that K_0 of Fe-(19,21)Si is markedly reduced relative to literature trends, while Fe-(10,15,29)Si are in good agreement. This is attributed to the fact that Fe-(19,21)Si are bcc-structured alloys well beyond the compositional stability field of this structure at ambient conditions. Thus, due to the suppression of Si ordering, K_0 of these materials is significantly reduced because of the increased influence of d - d screening relative to ordering on the cohesive properties of the alloys.

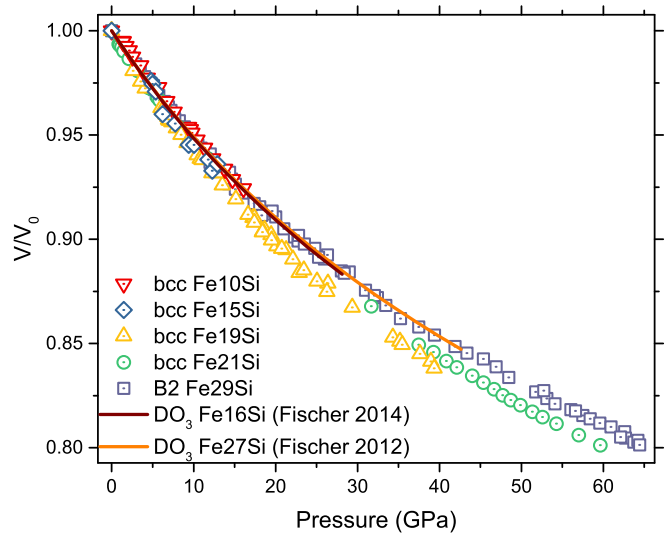


FIG. 6. Isothermal compression curves from the present study and modern literature [31,32].

Indeed, as shown in Fig. 6, while the Fe-(16,27)Si DO_3 structured alloys reported in Fischer *et al.* [31,32] have comparable compressibility to each other at high pressures, the alloys from the present study show significant variation of compressibility over the same compositional range.

C. Pressure derivative of the bulk modulus K' vs Si content

Across different literature investigations of the Fe-Si system, there has been little consensus on the evolution of K' with Si content due to scatter between different studies. Thanks to the high- P range and quality of the present data set, Fig. 7 shows that K' is roughly in the range of 5–5.5 for alloys Fe-(19,21,29)Si, in agreement with [31,32], and that the influence of Si ordering on K' is negligible within errors. Furthermore, a comparison of the K' of DAC experiments and single-crystal pulse-echo ultrasonics (SC-US) measurements for Fe and Fe-5Si shows that K' of these alloys are weakly dependent on Si concentration. However, this relation does not hold at higher Si concentrations, as B2 Fe-50Si has been observed to exhibit systematically lower K' ($K' = 4$ –4.5 [33,56]), while K' of B2 Fe-50Si is considerably higher ($K' \sim 6.6$ [32,35]).

D. Density dependence of sound velocities ($dV_p/d\rho$ and $dV_s/d\rho$) at high pressures

As sound velocities are highly sensitive to changes in both the shear and compressional moduli of a solid, the slopes of the V_p - and V_s -density plots are a key indicator for changes in the interatomic potential of solids as a function of composition and structure. It is observed in Fig. 8 that there is a weak increase in $dV_p/d\rho$ as a function of composition for the bcc-structured alloys and a significant increase in this quantity relative to bcc Fe associated with the B2 and B20 structures. The inset of Fig. 8 shows that while $dV_s/d\rho$ is essentially constant across the bcc alloys, $dV_p/d\rho$ observed for Fe-29Si and B20 Fe-50Si [35] are larger, as a direct consequence of modifications of the shear properties of the material. This observation supports the argument made by recent *ab initio*

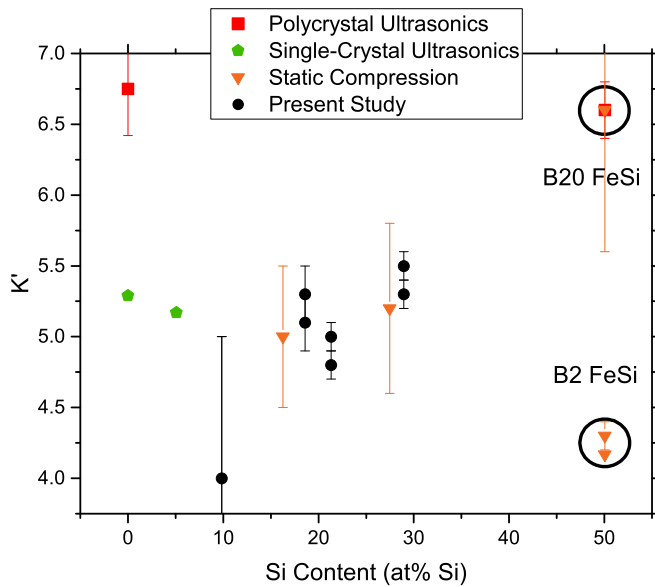


FIG. 7. K' vs Si content for the present study and available literature [30–35,41,42]. The two values for the same composition reported in the present study correspond to the results of fitting compressional data with the RV and 3BM formalisms. It is observed that this quantity is effectively constant with Si content up to 30 at. % Si irrespective of Si ordering.

calculations that changes in bond covalency, in competition with the magnetovolume effect, drive the observed anomalies in the elastic properties of Fe-Si alloys in the vicinity of the DO₃ transition [11]. An increase in covalency results in increased directionality of bonding, and this change in bonding typically enhances the shear modulus of the material (e.g., [66]), which could affect the variation of shear velocities with density.

E. The bcc-hcp phase transition at high pressures

In Fe-Si alloys, Si addition is known to stabilize the bcc phase relative to hcp at ambient temperature (e.g., [31,67]).

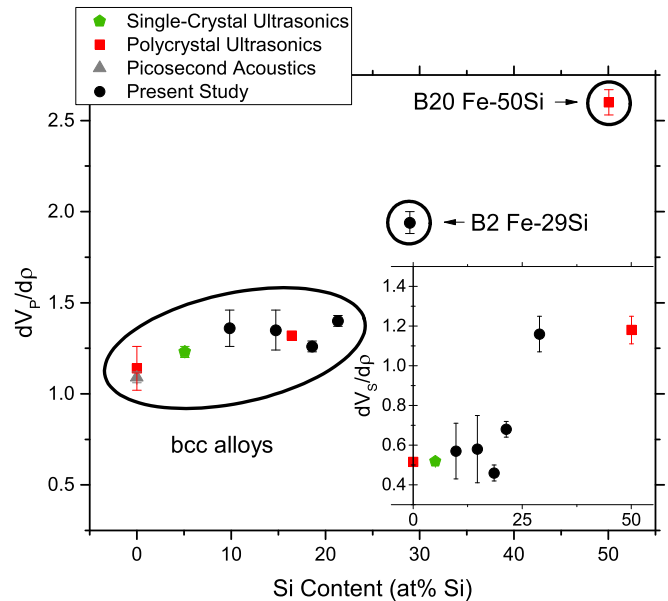
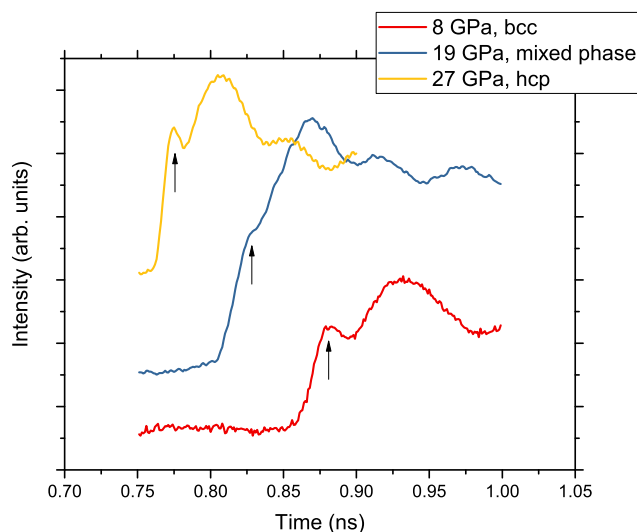


FIG. 8. $dV_p/d\rho$ vs Si content. Inset: $dV_s/d\rho$ vs Si content from the present study and available literature [30,35,38,41,42,44]. It is seen that there is good agreement across different studies and methods, with large changes corresponding primarily to changes in structure.

However, at present the variation of transition pressure with Si content is poorly constrained. In this study the bcc-hcp transition pressure and the extent of two-phase coexistence have been constrained using two metrics: the “smearing” of the first acoustic echo in time domain PA measurements and the direct observation of a mixed phase by XRD. Figure 9 shows the time domain PA measurements taken for alloys Fe-10Si and Fe-19Si. It is observed that within the bcc or hcp stability field, the first acoustic echo is sharp and well defined, while in contrast the mixed-phase region is characterized by a distortion of the shape and intensity of the first acoustic echo.

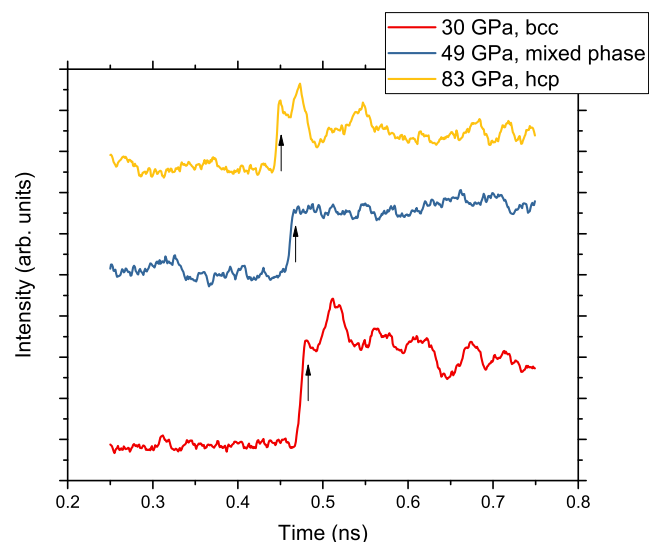


FIG. 9. Time domain PA measurements of Fe-10Si (left) and Fe-19Si (right) across the bcc-hcp transition.

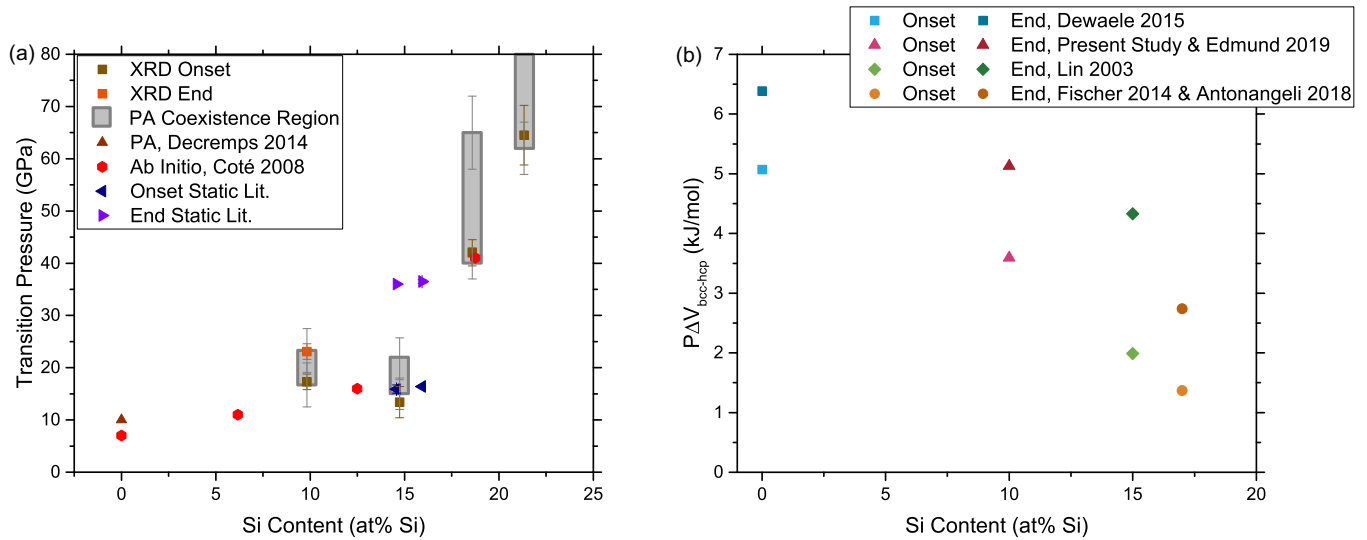


FIG. 10. (a) Pressure dependence of the bcc-hcp transition as a function of Si content (the end of the transition for Fe-21Si was not observed). (b) Pressure-volume work across the bcc-hcp transition vs Si content (right).

When this metric is applied for the determination of the onset and end of the bcc-hcp transition, PA measurements are in good agreement with structural determination via XRD [Fig. 10(a)]. This distortion of the acoustic echo is likely related to the fact that during the bcc-hcp transition the sample is a mechanical mixture of elastically distinct phases. In Fig. 10(a) it is shown that, in agreement with *ab initio* calculations [67], there is a weak increase in transition pressure for Fe-Si alloys containing up to 16 at. % Si, above which there is a significant increase in transition pressure. Between Fe-15Si and Fe-21Si there is a change in bcc-hcp transition pressure of ~ 7 GPa per at. % Si, and no transition is observed for Fe-29Si up to the highest investigated pressure. It has been shown that Si alloying acts to reduce the volume of bcc/B2/DO₃ Fe-Si alloys at constant pressure, while all the existing literature indicates that hcp Fe-Si alloys have a volume similar to or higher than that of hcp Fe at constant pressure (e.g., [18,32,55,68]). Thus, assuming that the free energy of the transition does not significantly change with Si content, the reduction in volume difference between the two phases necessitates a shift of the transition to higher pressures. It can be seen in Fig. 10(b) that based on the present work and existing literature [18,32,55,69,70], $P\Delta V$ (the pressure-volume work) of the bcc-hcp transition decreases with increasing Si content, indicating a reduction in the free-energy change in the transition with increasing Si content in the absence of an external hcp-stabilizing mechanism. Both the significant increase in transition pressure with Si content and decrease in $P\Delta V$ compare favorably with recent ramp compression studies, which show that for Fe-26Si there is no hcp phase of this alloy to at least 1.3 TPa [71]. It is noted, however, that the exact phase boundaries as identified by static and dynamic compression might vary, depending on the kinetics of diffusion and the timescales of dynamic compression experiments. For instance, the demixing of Fe-27Si into hcp and B2 structured alloys [31] is not reported in laser-driven dynamic ramp compression experiments [71]. Furthermore, the decrease in ΔV of the bcc-hcp transition

with increasing Si content at ambient temperature highlights the critical importance of differences in both thermoelasticity and entropy of the B2 and hcp phases to elucidate the boundaries between these phases at high P - T .

V. CONCLUSIONS

In summary, bcc and B2 Fe-Si alloys were investigated at ambient and elevated pressures by picosecond acoustics and synchrotron x-ray diffraction. The combined data sets show that the suppression of Si ordering in the DO₃ stability field by out-of-equilibrium synthesis methods results in significantly larger variability of the ambient-pressure bulk modulus than DO₃-structured Fe-Si alloys of the same composition. Despite the observed variation in K_0 , for Fe-Si alloys with Si content up to ~ 30 at. %, K' is essentially constant, irrespective of the degree of Si ordering. For Fe-Si alloys in the bcc structure, compositional variation of V_P and V_S with density is mostly driven by variation in $V_{P,S0}$ and ρ_0 . It follows that the variation of $dV_P/d\rho$ and $dV_S/d\rho$ with composition of the alloy is primarily a function of the structure of the alloy, which changes considerably between the bcc- and B2-structured alloys studied here. This observation indicates a strong influence of Si ordering on the alloy interatomic potential, which is posited to be due to an increase in bond covalency in Si-ordered Fe-Si solid solutions. Finally, the bcc-hcp transition in these alloys has been investigated by both PA and XRD, and it has been shown that there is a sharp increase in transition pressure above ~ 15 at. % Si, in agreement with *ab initio* calculations.

ACKNOWLEDGMENTS

This work was supported by the Investissements d'Avenir program (reference ANR-11-IDEX-0004-02) and more specifically within the framework of the Cluster of Excellence MATériaux Interfaces Surfaces Environnement (MATISSE) led by Sorbonne Université (grant to D.A. and F.D.).

Femtosecond laser micromachining at the Institut de Minéralogie, de Physique des Matériaux et de Cosmochimie (IMPMC), Paris, was developed and realized by the “Cellule Projet” with the financial support of ANR Grant No. 2010-JCJC-604-01 (grant to D.A.). The authors wish to thank M. Escudier, L. Becerra, and E. Dandeu at l’Institut des

Nanosciences de Paris (INSP) for assistance with profilometric measurements. Furthermore, the authors wish to thank N. Coudurier for help with SEM analysis. J. Jacobs is acknowledged for technical assistance at the ESRF. A. Polian, P. Paraskevas, and Y. Guarnelli are acknowledged for assistance with gas loading at IMPMC and Synchrotron SOLEIL.

- [1] F. González Cámara and Y. Houbaert, *Rev. Metal.* **49**, 178 (2013).
- [2] T. D. Yensen, *Univ. Ill. Bull.* **13**, 5 (1915).
- [3] I. Ohnuma, S. Abe, S. Shimenouchi, T. Omori, R. Kainuma, and K. Ishida, *ISIJ Int.* **52**, 540 (2012).
- [4] E. G. Moroni, W. Wolf, J. Hafner, and R. Podloucky, *Phys. Rev. B* **59**, 12860 (1999).
- [5] G. Phragmén, *J. Iron Steel Inst.* **114**, 397 (1926).
- [6] M. C. M. Farquhar, H. Lipson, and A. R. Weill, *J. Iron Steel Inst.* **152**, 457 (1945).
- [7] A. Machová and S. Kadečková, *Czech. J. Phys. B* **27**, 555 (1977).
- [8] A. R. Büchner and H. D. Kemnitz, *Z. Metallkd.* **72**, 575 (1981).
- [9] N. I. Kulikov, D. Fristot, J. Hugel, and A. V. Postnikov, *Phys. Rev. B* **66**, 014206 (2002).
- [10] T. Khmelevska, S. Khmelevskiy, A. V. Ruban, and P. Mohn, *J. Phys.: Condens. Matter* **18**, 6677 (2006).
- [11] S. K. Bhattacharya, M. Kohyama, S. Tanaka, Y. Shiihara, A. Saengdeejing, Y. Chen, and T. Mohri, *Mater. Res. Express* **4**, 116518 (2017).
- [12] W. J. Carr and R. Smoluchowski, *Phys. Rev.* **83**, 1236 (1951).
- [13] G. Tian and X. Bi, *J. Alloys Compd.* **502**, 1 (2010).
- [14] T. Jayaraman, V. Meka, X. Jiang, N. Overman, J. Doyle, J. Shield, and S. Mathaudhu, *J. Alloys Compd.* **741**, 409 (2018).
- [15] Edited by K. H. J. Buschow, *Handbook of Magnetic Materials*, 1st ed., Vol. 10 (North Holland, Amsterdam, 1997).
- [16] N. R. Overman, X. Jiang, R. K. Kukkadapu, T. Clark, T. J. Roosendaal, G. Coffey, J. E. Shield, and S. N. Mathaudhu, *Mater. Charact.* **136**, 212 (2018).
- [17] G. Morard, D. Andrault, N. Guignot, J. Siebert, G. Garbarino, and D. Antonangeli, *Phys. Chem. Miner.* **38**, 767 (2011).
- [18] E. Edmund, D. Antonangeli, F. Decremps, F. Miozzi, G. Morard, E. Boulard, A. N. Clark, S. Ayrinhac, M. Gauthier, M. Morand, and M. Mezouar, *J. Geophys. Res.: Solid Earth* **124**, 3436 (2019).
- [19] K. D. Litasov, P. I. Dorogokupets, E. Ohtani, Y. Fei, A. Shatskiy, I. S. Sharygin, P. N. Gavryushkin, S. V. Rashchenko, Y. V. Seryotkin, Y. Higo, K. Funakoshi, A. D. Chanyshev, and S. S. Lobanov, *J. Appl. Phys.* **113**, 093507 (2013).
- [20] R. Ross and W. Hume-Rothery, *J. Less-Common Met.* **5**, 258 (1963).
- [21] A. Dewaele, M. Torrent, P. Loubeyre, and M. Mezouar, *Phys. Rev. B* **78**, 104102 (2008).
- [22] T. Sokolova, P. Dorogokupets, and K. Litasov, *Russ. Geol. Geophys.* **54**, 181 (2013).
- [23] C. Prescher and V. B. Prakapenka, *High Press. Res.* **35**, 223 (2015).
- [24] P. Václav, D. Michal, and P. Lukáš, *Zeitschrift für Kristallographie - Crystalline Materials* **229**, 345 (2014).
- [25] Y. Seto, D. Nishio-Hamane, T. Nagai, and N. Sata, *Rev. High Pressure Sci. Technol.* **20**, 269 (2010).
- [26] F. Decremps, M. Gauthier, S. Ayrinhac, L. Bove, L. Belliard, B. Perrin, M. Morand, G. L. Marchand, F. Bergame, and J. Philippe, *Ultrasonics* **56**, 129 (2015).
- [27] H. K. Mao, J. Xu, and P. M. Bell, *J. Geophys. Res.* **91**, 4673 (1986).
- [28] P. Vinet, J. H. Rose, J. Ferrante, and J. R. Smith, *J. Phys.: Condens. Matter* **1**, 1941 (1989).
- [29] F. Birch, *Phys. Rev.* **71**, 809 (1947).
- [30] M. W. Guinan and D. N. Beshers, *J. Phys. Chem. Solids* **29**, 541 (1968).
- [31] R. A. Fischer, A. J. Campbell, R. Caracas, D. M. Reaman, P. Dera, and V. B. Prakapenka, *Earth Planet. Sci. Lett.* **357–358**, 268 (2012).
- [32] R. A. Fischer, A. J. Campbell, R. Caracas, D. M. Reaman, D. L. Heinz, P. Dera, and V. B. Prakapenka, *J. Geophys. Res.: Solid Earth* **119**, 2810 (2014).
- [33] N. Sata, K. Hirose, G. Shen, Y. Nakajima, Y. Ohishi, and N. Hirao, *J. Geophys. Res.* **115**, B09204 (2010).
- [34] S. Ono, *Phys. Earth Planet. Inter.* **224**, 32 (2013).
- [35] M. L. Whitaker, W. Liu, Q. Liu, L. Wang, and B. Li, *Am. Mineral.* **94**, 1039 (2009).
- [36] See Supplemental Material at <http://link.aps.org/supplemental/10.1103/PhysRevB.100.134105> for a table of experimental conditions achieved with XRD for each alloy (Table S1), collected literature elastic parameters for Fe-Si alloys (Table S2), examples of diffraction patterns of the studied alloys at ambient and high pressure (Graphs S1, S2 and S4), and V_s -density relations at high pressures from the present study (Graph S3).
- [37] S. Klotz and M. Braden, *Phys. Rev. Lett.* **85**, 3209 (2000).
- [38] F. Decremps, D. Antonangeli, M. Gauthier, S. Ayrinhac, M. Morand, G. L. Marchand, F. Bergame, and J. Philippe, *Geophys. Res. Lett.* **41**, 1459 (2014).
- [39] S. M. Dorfman, V. B. Prakapenka, Y. Meng, and T. S. Duffy, *J. Geophys. Res.* **117**, B08210 (2012).
- [40] J.-P. Poirier, *Introduction to the Physics of the Earth’s Interior* (Cambridge University Press, Cambridge, 2000), p. 326.
- [41] F. F. Voronov and E. V. Chernysheva, *Phys. Solid State* **41**, 462 (1999).
- [42] Y. Shibazaki, K. Nishida, Y. Higo, M. Igarashi, M. Tahara, T. Sakamaki, H. Terasaki, Y. Shimoyama, S. Kuwabara, Y. Takubo, and E. Ohtani, *Am. Mineral.* **101**, 1150 (2016).
- [43] J. Badro, G. Fiquet, F. Guyot, E. Gregoryanz, F. Occelli, D. Antonangeli, and M. d’Astuto, *Earth Planet. Sci. Lett.* **254**, 233 (2007).
- [44] L. Deng, Y. Kono, and G. Shen, *Am. Mineral.* **104**, 291 (2019).
- [45] D. Antonangeli and E. Ohtani, *Prog Earth Planet. Sci.* **2**, 3 (2015).

- [46] J. Shin, J. Bae, H. Kim, H. Lee, T. Lee, E. Lavernia, and Z. Lee, *Mater. Sci. Eng. A* **407**, 282 (2005).
- [47] S. Cui and I.-H. Jung, *CALPHAD* **56**, 108 (2017).
- [48] E. R. Jette and E. S. Greiner, *Am. Inst. Min. Metall. Eng.* **105**, 259 (1933).
- [49] G. H. Cockett and C. D. Davis, *J. Iron Steel Inst.* **201**, 110 (1963).
- [50] V. F. Lihl and H. Ebel, *Arch. Eisenhüttenwesen* **32**, 489 (1961).
- [51] E. R. Cohen and J. W. M. DuMond, *Rev. Mod. Phys.* **37**, 537 (1965).
- [52] M. Polcarová, S. Kadečková, J. Bradler, K. Godwod, and J. Bał-misiuk, *Phys. Status Solidi A* **106**, 17 (1988).
- [53] J. B. Rausch, Master's thesis, Iowa State University, 1976.
- [54] N. Hirao, E. Ohtani, T. Kondo, and T. Kikegawa, *Phys. Chem. Miner.* **31**, 329 (2004).
- [55] J.-F. Lin, V. V. Struzhkin, W. Sturhahn, E. Huang, J. Zhao, M. Y. Hu, E. E. Alp, H.-k. Mao, N. Boctor, and R. J. Hemley, *Geophys. Res. Lett.* **30**, 2112 (2003).
- [56] D. P. Dobson, W. A. Crichton, P. Bouvier, L. Vočadlo, and I. G. Wood, *Geophys. Res. Lett.* **30**, 14 (2003).
- [57] P. Shyni and P. Alagarsamy, *Phys. B (Amsterdam, Neth.)* **448**, 60 (2014), Selected Papers from International Conference on Magnetic Materials and Applications (MagMA-2013).
- [58] J. Karel, J. Juraszek, J. Minar, C. Bordel, K. H. Stone, Y. N. Zhang, J. Hu, R. Q. Wu, H. Ebert, J. B. Kortright, and F. Hellman, *Phys. Rev. B* **91**, 144402 (2015).
- [59] C. S. Wang, B. M. Klein, and H. Krakauer, *Phys. Rev. Lett.* **54**, 1852 (1985).
- [60] M. B. Stearns, *Phys. Rev.* **129**, 1136 (1963).
- [61] J. Zhang and F. Guyot, *Phys. Chem. Miner.* **26**, 206 (1999).
- [62] A. E. Petrova, V. N. Krasnorussky, A. A. Shikov, W. M. Yuhasz, T. A. Lograsso, J. C. Lashley, and S. M. Stishov, *Phys. Rev. B* **82**, 155124 (2010).
- [63] J. Routbort, C. Reid, E. Fisher, and D. Dever, *Acta Metall.* **19**, 1307 (1971).
- [64] L. S. Dubrovinsky, S. K. Saxena, N. A. Dubrovinskaia, S. Rekhii, and T. Le Bihan, *Am. Mineral.* **85**, 386 (2000).
- [65] O. G. Randl, G. Vogl, W. Petry, B. Hennion, B. Sepiol, and K. Nembach, *J. Phys.: Condens. Matter* **7**, 5983 (1995).
- [66] J. Haines, J. Léger, and G. Bocquillon, *Annu. Rev. Mater. Res.* **31**, 1 (2001).
- [67] A. S. Côté, L. Vočadlo, and J. P. Brodholt, *J. Phys. Chem. Solids* **69**, 2177 (2008), Study of Matter Under Extreme Conditions 2007.
- [68] A. Dewaele, P. Loubeyre, F. Occelli, M. Mezouar, P. I. Dorogokupets, and M. Torrent, *Phys. Rev. Lett.* **97**, 215504 (2006).
- [69] A. Dewaele, C. Denoual, S. Anzellini, F. Occelli, M. Mezouar, P. Cordier, S. Merkel, M. Véron, and E. Rausch, *Phys. Rev. B* **91**, 174105 (2015).
- [70] D. Antonangeli, G. Morard, L. Paolasini, G. Garbarino, C. A. Murphy, E. Edmund, F. Decremps, G. Fiquet, A. Bosak, M. Mezouar, and Y. Fei, *Earth Planet. Sci. Lett.* **482**, 446 (2018).
- [71] J. K. Wicks, R. F. Smith, D. E. Fratanduono, F. Coppari, R. G. Kraus, M. G. Newman, J. R. Rygg, J. H. Eggert, and T. S. Duffy, *Sci. Adv.* **4**, eaao5864 (2018).